A regularized Newton method for locating thin tubular conductivity inhomogeneities

2011 Inverse Problems 27 115008

(http://iopscience.iop.org/0266-5611/27/11/115008)

Inverse Problems **27** (2011) 115008 (22pp) doi:10.1088/0266-5611/27/11/115008

A regularized Newton method for locating thin tubular conductivity inhomogeneities

Roland Griesmaier[1] **and Nuutti Hyvönen**[2]

[1] Institut für Mathematik, Johannes Gutenberg-Universität, Staudingerweg 9, 55099 Mainz, Germany
[2] Department of Mathematics and Systems Analysis, Aalto University, PO Box 11100, FI-00076 Aalto, Finland

E-mail: griesmai@uni-mainz.de and nuutti.hyvonen@hut.fi

Received 9 March 2011, in final form 17 July 2011
Published 21 October 2011
Online at stacks.iop.org/IP/27/115008

Abstract
We consider the inverse problem of determining the position and shape of a thin tubular object, such as for instance a wire, a thin channel or a curve-like crack, embedded in some three-dimensional homogeneous body from a single measurement of electrostatic currents and potentials on the boundary of the body. Using an asymptotic model describing perturbations of electrostatic potentials caused by such thin objects, we reformulate the inverse problem as a nonlinear operator equation. We establish Fréchet differentiability of the corresponding operator, compute its Fréchet derivative and set up a regularized Newton scheme to solve the inverse problem numerically. We discuss our implementation of this method and present numerical results for simulated forward data.

(Some figures may appear in colour only in the online journal)

1. Introduction

In this paper, we investigate the inverse problem to reconstruct a thin curve-like object contained in some otherwise homogeneous three-dimensional body from measurements of electrostatic currents and potentials on the boundary of this body. More precisely, we assume that a three-dimensional bounded domain that is filled with a homogeneous background medium of constant electric conductivity contains a thin neighborhood of some smooth curve, where the conductivity differs from that of the background medium. This thin tubular subdomain will be called conductivity inhomogeneity or simply inclusion. If now an electric current is applied on the boundary of the domain, then the conductivity inhomogeneity affects the resulting electrostatic potential, and this effect depends nonlinearly on the position and shape of the inclusion. The inverse problem we want to study attempts to reconstruct

the position and shape of an unknown inclusion, given a single boundary current and the corresponding potential on the boundary of the domain.

To begin with, we note that since the conductivity inhomogeneity is assumed to be thin, i.e. its volume is small compared to the volume of the body itself, the effect of the conductivity inhomogeneity on the electrostatic potential on the boundary of the domain is relatively small (see, e.g., Capdeboscq and Vogelius [7]). This smallness causes one of the main difficulties when trying to recover such inclusions in practice because it first of all requires the electric current and potential on the boundary to be measured with sufficiently high accuracy. This issue will be further addressed in our numerical examples at the end of this work.

An inverse problem that is related to our work and has been widely studied in recent years is crack identification, i.e. the reconstruction of perfectly conducting, insulating or imperfectly conducting hypersurfaces in two- or three-dimensional domains (see, e.g., the recent review article by Bryan and Vogelius [5], or Brühl *et al* [4], Cakoni and Colton [6], Kirsch and Ritter [14], and Kress *et al* [13, 15–17]). These cracks are usually modeled as interior boundaries, carrying Dirichlet-, Neumann- or impedance boundary conditions for the potential. Since in contrast to the two-dimensional case one-dimensional curves in three-dimensional domains do not support well-defined boundary conditions, a corresponding model for curve-like inclusions in three-dimensional domains is not available. Therefore, a straightforward generalization of inversion algorithms developed for crack detection problems to the inverse problem considered here is not feasible, even if the inclusions would be insulating or perfectly conducting.

The reconstruction method studied in this work relies on an asymptotic representation formula describing perturbations of electrostatic potentials on the boundary of the domain caused by thin tubular conductivity inhomogeneities as their volume tends to zero. This formula is a special case of a much more general result established in [7] and further analyzed in [8, 9]. Assuming that the volume of the inclusion is small relative to the volume of the whole domain, we identify the given data for the electrostatic potential on the boundary with the leading order term in this asymptotic perturbation formula. The dependence of this leading order term on the geometry and material properties of the inclusion is encoded in the so-called polarization tensor. To obtain an explicit description of this term, we formally generalize the pointwise spectral characterization of polarization tensors corresponding to thin straight tubular conductivity inhomogeneities recently established by Beretta *et al* [3] to arbitrarily curved thin tubular inclusions. Based on this characterization we discuss a class of boundary currents such that measurements of a single electrostatic potential corresponding to any of these boundary currents uniquely determine the position and shape of the conductivity inhomogeneity within the asymptotic model. Reformulating the inverse problem as a nonlinear operator equation, we compute the Fréchet derivative of the corresponding operator with respect to the position and shape of the inclusion and derive a regularized Newton scheme to solve the equation numerically.

Since our reconstruction method is formulated in terms of the leading order term of the asymptotic expansion of the boundary perturbation of the electrostatic potential, which is described by an explicit formula, the operator as well as its Fréchet derivative can be evaluated very efficiently in each step of the Newton iteration. Besides the fact that the algorithm by construction uses *a priori* information on the shape of the unknown inclusion, this efficiency and the few input data are the main advantages of this method.

To put our findings into a historical perspective, we note that a reconstruction method to recover the end points of thin straight tubular inclusions based on the asymptotic perturbation formula from [7] has recently been proposed in [3]. This method generalizes an earlier algorithm studied by Ammari *et al* [1, 2] for a corresponding problem in two dimensions. Furthermore, a non-iterative method to reconstruct arbitrarily shaped thin tubular conductivity

inhomogeneities in three-dimensional domains that relies on the asymptotic analysis from [7] has been investigated theoretically and implemented in [12]. In contrast to the present work, this method uses not only a single pair of Cauchy data but a finite approximation of the whole Neumann-to-Dirichlet map. A MUSIC-type reconstruction method and a level set method for a similar two-dimensional inverse scattering problem have been studied by Park and Lesselier [19–21].

This paper is organized as follows: in the next section, we introduce our mathematical setting and discuss the asymptotic representation formula for the boundary voltage perturbation caused by thin tubular inclusions. Section 3 is concerned with the inverse problem and the question which boundary currents are appropriate for the reconstruction of thin tubular inclusions. We rewrite the inverse problem as a nonlinear operator equation and show Fréchet differentiability of the corresponding operator in section 4. The Newton-type reconstruction method is explained in section 5, and numerical examples can be found in section 6.

2. The direct problem with thin tubular inclusions

We start by introducing our mathematical setting. Let $\Omega \subset \mathbb{R}^3$ be a bounded domain with smooth boundary $\partial\Omega$ and unit outward normal ν. Suppose that Ω is filled with a homogeneous background medium with constant background conductivity $\gamma_0 > 0$ and that it contains a thin tubular neighborhood

$$\omega_\varepsilon := \{x \in \Omega \mid \operatorname{dist}(x, K) < \varepsilon\} \tag{1}$$

of a C^2-curve $K \subset \Omega$, where the conductivity differs from the background conductivity and equals some other constant $\kappa > 0$. Here we assume that K is non-self-intersecting and either contains its endpoints or is closed and that $0 < \varepsilon < \varepsilon_0$ is small enough such that $\omega_\varepsilon \subset\subset \Omega$ is non-self-intersecting as well. So the conductivity distribution in the presence of the conductivity inhomogeneity ω_ε is given by

$$\gamma_\varepsilon(x) := \begin{cases} \kappa, & x \in \omega_\varepsilon, \\ \gamma_0, & x \in \Omega \setminus \overline{\omega_\varepsilon}, \end{cases} \tag{2}$$

and applying a normal boundary current flow

$$f \in L^2_\diamond(\partial\Omega) := \left\{ \phi \in L^2(\partial\Omega) \;\middle|\; \int_{\partial\Omega} \phi \, \mathrm{d}s = 0 \right\}$$

on $\partial\Omega$, the induced electrostatic potential u_ε in Ω satisfies the boundary value problem

$$\nabla \cdot (\gamma_\varepsilon \nabla u_\varepsilon) = 0 \quad \text{in} \quad \Omega, \tag{3a}$$

$$\gamma_\varepsilon \frac{\partial u_\varepsilon}{\partial \nu} = f \quad \text{on} \quad \partial\Omega. \tag{3b}$$

More precisely, we consider in this work the unique weak solution of (3) in

$$H^1_\diamond(\Omega) := \left\{ u \in H^1(\Omega) \;\middle|\; \int_{\partial\Omega} u \, \mathrm{d}s = 0 \right\}.$$

Replacing γ_ε by γ_0 in (3) yields the so-called background potential u_0.

Throughout this paper, we assume that the radius ε of the inclusion ω_ε is small relative to its length and its distance from the boundary $\partial\Omega$. The inverse problem we are studying is to reconstruct the position and shape of ω_ε, i.e. essentially its base curve K from one set of Cauchy data $(f, u_\varepsilon|_{\partial\Omega}) \in L^2_\diamond(\partial\Omega) \times L^2_\diamond(\partial\Omega)$. Our analysis relies on an asymptotic perturbation formula describing the asymptotic behavior of $u_\varepsilon|_{\partial\Omega}$ as ε tends to zero, i.e. as the conductivity inhomogeneity shrinks to the curve K. By working with this formula, we incorporate prior

information on the shape of the unknown inclusion, i.e. that we are searching for thin curve-like objects into the reconstruction method.

Before we recall the main results of the asymptotic analysis from [7] applied to our setting, we introduce the Neumann function N for the differential operator $\nabla \cdot \gamma_0 \nabla$ in Ω, which for any $y \in \Omega$ is the distributional solution of the boundary value problem

$$\nabla_x \cdot (\gamma_0(x) \nabla_x N(x, y)) = -\delta_y(x), \quad x \in \Omega, \tag{4a}$$

$$\gamma_0(x) \frac{\partial N(x, y)}{\partial \nu(x)} = -\frac{1}{|\partial\Omega|}, \quad x \in \partial\Omega, \tag{4b}$$

together with $\int_{\partial\Omega} N(x, \cdot)\, \mathrm{d}s(x) = 0$.

The following theorem can be deduced from the much more general theorem 1 in [7] by Capdeboscq and Vogelius as outlined in [12].

Theorem 2.1. *Let $K \subset \Omega$ be a simple C^2-curve and consider a sequence of inclusions $(\omega_{\varepsilon_n})_{n\in\mathbb{N}}$ as in (1), where $(\varepsilon_n)_{n\in\mathbb{N}}$ is a sequence in $(0, \varepsilon_0)$ converging to zero such that these inclusions are well defined and strictly contained in Ω. Denoting by γ_{ε_n}, $n \in \mathbb{N}$, the corresponding conductivity distributions as in (2), let u_{ε_n} be the associated solutions of (3) with boundary values $f \in L^2_\diamond(\partial\Omega)$ and let u_0 be the corresponding background solution. Then, there exists a subsequence, again denoted by $(\omega_{\varepsilon_n})_{n\in\mathbb{N}}$, and a matrix-valued function $\mathbb{M}_K \in L^2(K; \mathbb{R}^{3\times 3})$, called the polarization tensor, such that*

$$u_{\varepsilon_n}(y) = u_0(y) + \varepsilon_n^2 \pi \int_K (\gamma_0 - \kappa) \nabla_x N(x, y) \cdot \mathbb{M}_K(x) \nabla u_0(x)\, \mathrm{d}s(x) + o\big(\varepsilon_n{}^2\big) \tag{5}$$

for $y \in \partial\Omega$ as $n \to \infty$. The polarization tensor $\mathbb{M}_K$ is independent of f and its values are symmetric and positive definite matrices almost everywhere on K.

Theorem 2.1 is stated in terms of subsequences because for very general geometries as considered in [7], different subsequences might lead to different polarization tensors. However, for the special case of thin straight cylindrical inclusions, i.e. inclusions as in (1) but assuming that the base curve K is a straight line segment, Beretta *et al* [3] recently showed that the polarization tensor is independent of the particular subsequence. Furthermore, the following pointwise spectral characterization has been established in this special case: for almost every $x \in K$, the unit tangent vector $\boldsymbol{t}_K(x)$ to K at x is an eigenvector of the positive definite symmetric matrix $\mathbb{M}_K(x)$ corresponding to the eigenvalue 1 and its orthogonal complement is a two-dimensional eigenspace of $\mathbb{M}_K(x)$ corresponding to the eigenvalue $2\gamma_0/(\gamma_0 + \kappa)$. In fact, the result from [3] is more general, characterizing the polarization tensor of thin straight tubular inclusions with arbitrary cross-sections.

In the numerical reconstruction method described in this work, we approximate arbitrary C^2-curves K by piecewise linear splines and accordingly we approximate the polarization tensor $\mathbb{M}_K$ locally on K by the polarization tensor corresponding to a thin straight cylindrical conductivity inhomogeneity around the corresponding spline segment applying the pointwise spectral characterization from [3]. In the limit, as the number of spline segments tends to infinity, this means that we assume that the unit tangent vector $\boldsymbol{t}_K(x)$ to K at x is an eigenvector of $\mathbb{M}_K(x)$ corresponding to the eigenvalue 1 and its orthogonal complement is a two-dimensional eigenspace of $\mathbb{M}_K(x)$ corresponding to the eigenvalue $2\gamma_0/(\gamma_0 + \kappa)$—at least approximately. The following numerical example supports this procedure.

Example 2.2. For $\Omega := B_1(0)$ being the unit ball in $\mathbb{R}^3$, the Neumann function is known explicitly and given by

$$N(x, y) = \frac{1}{4\pi\gamma_0} \left(\frac{1}{|x - y|} + \frac{1}{\big||y|x - \frac{y}{|y|}\big|} + \log\left(\frac{2}{1 - x \cdot y + \big||y|x - \frac{y}{|y|}\big|} \right) \right), \quad x \neq y. \tag{6}$$

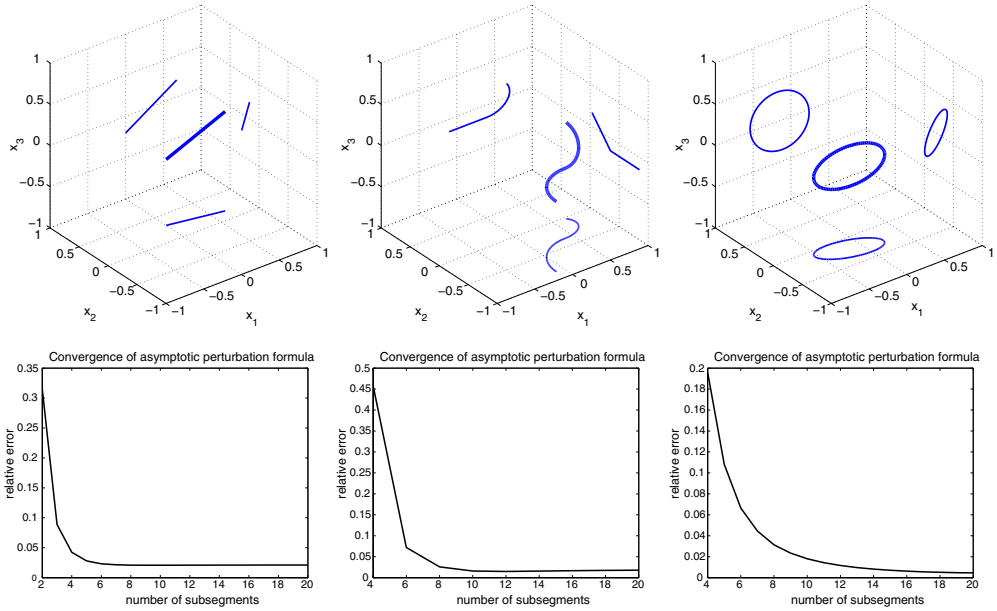

Figure 1. Top row: curves defining three thin tubular inclusions. Bottom row: relative difference between the finite element approximation and the asymptotic perturbation formula with respect to the number of subsegments used in the discretization of the asymptotic formula.

Furthermore, the background potential corresponding to the boundary current $f(x) := \nu(x) \cdot (1, 0, 0) = x_1$, $x \in \partial\Omega$, and the background conductivity $\gamma_0 = 1$ is just $u_0 = x_1$, $x \in \Omega$. We consider three thin tubular conductivity inhomogeneities in Ω, as sketched in figure 1 (top row). The first inclusion (top left) is a thin cylinder of radius $\varepsilon = 0.03$ and conductivity $\kappa = 0.4$, the second inclusion (top middle) is a thin tube of radius $\varepsilon = 0.01$ and conductivity $\kappa = 10$, composed of two circular arcs, and the third inclusion (top right) is a thin torus with a tube of radius $\varepsilon = 0.02$ and conductivity $\kappa = 2$. These images also show the projections of the inclusions onto the coordinate planes, which is a convention that is used in most of our figures.

Simulating the boundary perturbation $(u_\varepsilon - u_0)|_{\partial\Omega}$ for all three inclusions numerically with high accuracy using the finite element software Comsol, we interpolate this approximation on a grid of boundary points $Y = (y_{kl})_{kl} \subset \partial\Omega$,

$$y_{kl} = (\sin\theta_k \cos\phi_l,\ \sin\theta_k \sin\phi_l,\ \cos\theta_k), \qquad 1 \leqslant k \leqslant N-1,\ 1 \leqslant l \leqslant 2N, \tag{7}$$

with $\theta_k = k\pi/N$ and $\phi_l = l\pi/N$ for $N = 10$, and store these data in a vector $g_{\text{fem}} \in \mathbb{R}^{180}$.

Next, we evaluate the leading order term in the asymptotic expansion of $(u_\varepsilon - u_0)|_{\partial\Omega}$ according to (5). To this end, we approximate the curve K by a piecewise linear spline of the form

$$K \approx \bigcup_{j=1}^{n} [x^j, x^{j+1}],$$

where $\{x^j\}_{j=1}^{n+1} \subset K$ is a set of equidistant nodes (with respect to the arc length of K) and $[x^j, x^{j+1}]$ denotes the closed line segment between x^j and x^{j+1}. The integral over K is approximated by applying the trapezoid rule on each subsegment $[x^j, x^{j+1}]$ and evaluating

the polarization tensor in the nodes of this quadrature rule using the pointwise spectral characterization mentioned before. Collecting the values of this approximation on the boundary grid Y, we obtain a vector $g_{\text{asy}} \in \mathbb{R}^{180}$.

Visualizations of the relative difference $|g_{\text{fem}} - g_{\text{asy}}|_w / |g_{\text{fem}}|_w$ of these approximations with respect to the number of panels in the composite trapezoid rule are shown in figure 1 (bottom row). Here $|\cdot|_w$ denotes a weighted ℓ^2-norm of $\mathbb{R}^{180}$ with the corresponding weights $w \in \mathbb{R}^{180}$ chosen such that this quotient approximates the relative $L^2(\partial\Omega)$-norm of the difference between the finite element approximation and the leading order term in the asymptotic expansion. The relative difference decays nicely until it reaches its minimum around 0.02 (bottom-left), 0.015 (bottom-middle) and 0.005 (bottom-right). Note that due to the asymptotic character of the expansion (5) and due to numerical errors in the finite element approximation, we cannot expect the relative difference to be exactly zero. The results for the two curved thin inclusions are even better than for the straight thin inclusion for which the pointwise spectral characterization of the polarization tensor is known to hold exactly.

The previous example suggests that the pointwise spectral characterization of the polarization tensor corresponding to thin straight tubular inclusions from [3] applied to arbitrarily curved thin tubular inclusions yields satisfactory results. Thus, we assume in the following that the polarization tensor $\mathbb{M}_K$ in theorem 2.1 is independent of the particular subsequence and that for almost every $x \in K$, the unit tangent vector $\boldsymbol{t}_K(x)$ for K at x is an eigenvector of $\mathbb{M}_K(x)$ corresponding to the eigenvalue 1 and its orthogonal complement in $\mathbb{R}^3$ is a two-dimensional eigenspace of $\mathbb{M}_K(x)$ corresponding to the eigenvalue $2\gamma_0/(\gamma_0 + \kappa)$.

Remark 2.3. The asymptotic expansion (5) in theorem 2.1 is formulated in terms of the Neumann function N from (4), which might be difficult to evaluate for arbitrary domains Ω. In this case, as outlined in [7, remark 3], the perturbation formula can be rewritten in terms of the rescaled fundamental solution $\Phi(x, y) := \frac{1}{4\pi\gamma_0|x-y|}$ as follows:

$$(u_{\varepsilon_n} - u_0)(y) - 2\gamma_0 \int_{\partial\Omega} (u_{\varepsilon_n} - u_0)(x) \frac{\partial\Phi}{\partial\nu_x}(x, y)\, \mathrm{d}s(x)$$
$$= 2\varepsilon_n^2 \pi \int_K (\gamma_0 - \kappa) \nabla_x \Phi(x, y) \cdot \mathbb{M}_K(x) \nabla u_0(x)\, \mathrm{d}s(x) + o\big(\varepsilon_n{}^2\big)$$

for $y \in \partial\Omega$ as $n \to \infty$.

The reconstruction method developed in the following sections can be adapted to this representation formula straightforwardly. However, to simplify the presentation we choose to formulate the method in terms of the Neumann function.

3. The inverse problem

We consider in the following the inverse problem of reconstructing the base curve K corresponding to a conductivity inhomogeneity ω_ε as in (1) from one pair of boundary data $(f, u_\varepsilon|_{\partial\Omega})$. As we have observed in example 2.2, the perturbation in the boundary potential $(u_\varepsilon - u_0)|_{\partial\Omega}$ due to thin tubular conductivity inhomogeneities is well approximated by the leading order term in the asymptotic expansion (5),

$$g_\varepsilon(y) := \varepsilon^2 \pi \int_K (\gamma_0 - \kappa) \nabla_x N(x, y) \cdot \mathbb{M}_K(x) \nabla u_0(x)\, \mathrm{d}s(x), \qquad y \in \partial\Omega, \quad (8)$$

if ε is small enough. Therefore, assuming that the background potential $u_0|_{\partial\Omega}$ can be simulated sufficiently accurately during the reconstruction process given the shape of the domain Ω and estimating the background conductivity γ_0, the inverse problem reduces essentially to

reconstructing K given one pair (f, g_ε). In practice, this means that $u_\varepsilon|_{\partial\Omega}$ has to be known with high accuracy, in order to be able to obtain a reliable approximation $(u_\varepsilon - u_0)|_{\partial\Omega}$ of g_ε. If this is not feasible, i.e. if one cannot tell the difference in the boundary potentials with and without inclusion, the inverse problem to recover the position of ω_ε cannot be solved, regardless of which method is used.

Before we develop the reconstruction method, we discuss how to choose the boundary current f such that one pair (f, g_ε) uniquely determines the curve K—at least theoretically. To this end, we define the class of admissible boundary currents X to be the set of all $f \in L^2_\diamond(\partial\Omega)$ such that the corresponding background potential u_0 satisfies the following conditions.

- The gradient ∇u_0 does not vanish in Ω.
- There is no C^2-curve $\Gamma \subset \Omega$, except possibly straight line segments, such that $\nabla u_0 - (\boldsymbol{t}_\Gamma \cdot \nabla u_0)\boldsymbol{t}_\Gamma = 0$ on Γ and $\partial^2 u_0/\partial \boldsymbol{t}_\Gamma^2 = 0$ on Γ, where $\boldsymbol{t}_\Gamma$ denotes the unit tangent vector field along Γ.

Note that the set X is not empty; for instance, $f(x) := \nu(x) \cdot p|_{\partial\Omega} \in X$ for every $p \in \mathbb{R}^3 \setminus \{0\}$.

The following proposition generalizes a uniqueness result for thin straight tubular inclusions established in [3], assuming that the pointwise spectral characterization for the polarization tensor $\mathbb{M}_K$ holds for arbitrarily curved thin tubular inclusions.

Proposition 3.1. *Suppose K_1 and K_2 are two C^2-curves in Ω and let $\gamma_{\varepsilon,1}$ and $\gamma_{\varepsilon,2}$ be the corresponding conductivity distributions as in (2) with κ replaced by $0 < \kappa_1, \kappa_2 \neq \gamma_0$, respectively. We denote by $g_{\varepsilon,1}$ and $g_{\varepsilon,2}$ the leading order terms of the associated differences of the boundary potentials with and without inclusions as in (8), respectively, corresponding to an admissible boundary current $f \in X$, and assume that the pointwise spectral characterization of the polarization tensor holds. Then, $g_{\varepsilon,1}|_\Sigma = g_{\varepsilon,2}|_\Sigma$ on some nonempty open subset $\Sigma \subset \partial\Omega$ implies $K_1 = K_2$.*

Proof. Assume that $g_{\varepsilon,1}|_\Sigma = g_{\varepsilon,2}|_\Sigma$ on some nonempty open subset $\Sigma \subset \partial\Omega$. The canonical extensions of the boundary data $g_{\varepsilon,i}$, $i = 1, 2$, to $\Omega \setminus K_i$ given by

$$v_{\varepsilon,i}(y) := \varepsilon^2 \pi \int_{K_i} (\gamma_0 - \kappa)\nabla_x N(x, y) \cdot \mathbb{M}_{K_i}(x)\nabla u_0(x)\, \mathrm{d}s(x), \qquad y \in \Omega \setminus K_i,$$

satisfy $\Delta v_{\varepsilon,i} = 0$ in $\Omega \setminus (K_1 \cup K_2)$ and have vanishing Neumann data on $\partial\Omega$. Since their Cauchy data coincide on the open subset $\Sigma \subset \partial\Omega$, we conclude that $v_{\varepsilon,1} = v_{\varepsilon,2}$ in $\Omega \setminus (K_1 \cup K_2)$ (cf, e.g., Dautray and Lions [10, corollary 11, p 262]). Furthermore, $v_{\varepsilon,1}$ is smooth in $\Omega \setminus K_1$ and $v_{\varepsilon,2}$ is smooth in $\Omega \setminus K_2$. Now assume that $K_1 \neq K_2$ and without loss of generality $K_2 \setminus K_1 \neq \emptyset$. We show that there exists $z \in K_2 \setminus K_1$ and a direction $a \in \mathbb{R}^3 \setminus \{0\}$ such that $\lim_{t\to 0} |v_{\varepsilon,2}(z + ta)| = \infty$. This yields a contradiction because $v_{\varepsilon,2}$ coincides with $v_{\varepsilon,1}$ in $\Omega \setminus (K_1 \cup K_2)$ and therefore is uniformly bounded in a neighborhood of $z \in \Omega \setminus K_1$.

Denoting by $\boldsymbol{t}_{K_2}$ the unit tangent vector for K_2 and by $\mathbb{M}_{K_2}$ the polarization tensor corresponding to the conductivity inhomogeneities described by $\gamma_{\varepsilon,2}$, $0 < \varepsilon < \varepsilon_0$, we write $\phi := \mathbb{M}_{K_2}\nabla u_0$ on $K_2 \setminus K_1$ and decompose $\phi = \phi_n + \phi_t$, where $\phi_t := (\phi \cdot \boldsymbol{t}_{K_2})\boldsymbol{t}_{K_2}$ and accordingly $\phi_n := \phi - \phi_t$. From the spectral decomposition of $\mathbb{M}_{K_2}$, we find that

$$\phi_t = (\nabla u_0 \cdot \boldsymbol{t}_{K_2})\boldsymbol{t}_{K_2} \qquad \text{and} \qquad \phi_n = \frac{2\gamma_0}{\gamma_0 + \kappa_2}\big(\nabla u_0 - (\boldsymbol{t}_{K_2} \cdot \nabla u_0)\boldsymbol{t}_{K_2}\big).$$

Furthermore, rewriting the Neumann function for each $y \in \Omega$ as

$$N(\cdot, y) = \frac{1}{4\pi\gamma_0}\frac{1}{|\cdot - y|} + R_N(\cdot, y),$$

where $R_N(\cdot, y)$ is a smooth function in Ω (cf, e.g., [11]), we can use partial integration, denoting the endpoints of the curve K_2 by P and Q, to obtain for $y \notin K_2$

$$v_{\varepsilon,2}(y) = \varepsilon^2 \pi (\gamma_0 - \kappa) \Bigg(\big(\nabla u_0 \cdot \boldsymbol{t}_{K_2}\big)(Q)\Phi(Q, y) - \big(\nabla u_0 \cdot \boldsymbol{t}_{K_2}\big)(P)\Phi(P, y) - \int_{K_2} \frac{\partial^2 u_0}{\partial \boldsymbol{t}_{K_2}^2} \Phi(x, y)\, \mathrm{d}s(x) + \int_{K_2} \phi_n(x) \cdot \nabla \Phi(x, y)\, \mathrm{d}s(x) + \int_{K_2} \phi(x) \cdot \nabla R_N(x, y)\, \mathrm{d}s(x) \Bigg). \tag{9}$$

Now we distinguish two cases. First suppose that $K_2 \setminus K_1$ and $K_1 \setminus K_2$ are straight line segments or $K_2 \setminus K_1$ is a straight line segment and $K_1 \setminus K_2 = \emptyset$. In this case, we can choose $z \in K_2 \setminus K_1$ to be an endpoint of K_2 and $a_1 \in \{\pm \boldsymbol{t}_K(z)\}$ and $\tau_1 > 0$ such that the straight line segment $\Gamma_1 := \{z + t a_1 \mid 0 < t \leqslant \tau_1\} \subset \Omega \setminus (K_1 \cup K_2)$. Similar to the proof of proposition 3.2 in [12] (see also [3, proposition 4.1]), we can estimate each term in (9) separately to see that

$$\big|v_{\varepsilon,2}(z + t a_1)\big| \geqslant C |(\nabla u_0 \cdot \boldsymbol{t}_{K_2})(z)| \frac{1}{t} + O(\log(t^{-1})) \qquad \text{as } t \to 0.$$

Therefore, recalling that $v_{\varepsilon,2}(z + t a_1) = v_{\varepsilon,1}(z + t a_1)$ is bounded around $z \in \Omega \setminus K_1$, we conclude that $(\nabla u_0 \cdot \boldsymbol{t}_{K_2})(z) = 0$. Now, according to our assumption $\nabla u_0(z) \neq 0$, we find that $\phi_n(z) \neq 0$ and we can choose a second direction $a_2 := \phi_n(z)/|\phi_n(z)|$ and $\tau_2 > 0$ such that the straight line segment $\Gamma_2 := \{z + t a_2 \mid 0 < t \leqslant \tau_2\} \subset \Omega \setminus (K_1 \cup K_2)$. Again estimating each term in (9) as done in [12, proposition 3.2], it follows that

$$\big|v_{\varepsilon,2}(z + t a_2)\big| \geqslant C \big|\phi_n(z)\big| \frac{1}{t} + O(\log(t^{-1})) \qquad \text{as} \quad t \to 0,$$

which implies again by the boundedness of $v_{\varepsilon,2}$ around $z \in \Omega \setminus K_1$ that $\phi_n(z) = 0$, i.e. a contradiction, and ends the proof in this case.

In the second case, we assume that $K_2 \setminus K_1$ is not a straight line segment (otherwise we interchange the roles of K_1 and K_2). According to the definition of the class of admissible boundary currents X above, we can choose $z \in K_2 \setminus K_1$ such that $\phi_n(z) \neq 0$ or $(\partial^2 u_0/\partial \boldsymbol{t}_{K_2}^2)(z) \neq 0$. Now let $a_3 := \phi_n(z)/|\phi_n(z)|$ if $\phi_n \neq 0$ or $a_3 \in \mathbb{R}^3 \setminus \{0\}$ such that $a_3 \cdot \boldsymbol{t}_{K_2}(z) = 0$ otherwise and consider the straight line segment $\Gamma_3 := \{z + t a_3 \mid 0 < t \leqslant \tau_3\}$, where $\tau_3 > 0$ is such that $\Gamma_3 \subset \Omega \setminus (K_1 \cup K_2)$. Then, following once more the proof of [12, proposition 3.2], we can estimate each term in (9) to obtain

$$|v_{\varepsilon,2}(z + t a_3)| \geqslant C_1 \frac{\partial^2 u_0}{\partial \boldsymbol{t}_{K_2}^2}(z) \log(t^{-1}) + C_2 |\phi_n(z)| \left(\frac{1}{t} + O(\log(t^{-1}) \right) + O(1).$$

Therefore, we conclude that $\lim_{t \to 0} |v_{\varepsilon,2}(z + t a_3)| = \infty$, which is a contradiction and ends the proof. □

From now on let $f \in X$ be an admissible boundary current, denote by u_0 the corresponding background potential and by u_ε the solution of (3). Introducing an operator $\mathcal{T} : K \mapsto g_\varepsilon$ that maps the curve K to the leading order term g_ε from (8) of the asymptotic expansion (5), our inverse problem essentially amounts to solving the nonlinear operator equation

$$\mathcal{T}(K) = g_\varepsilon \tag{10}$$

for the unknown curve K. We will use a regularized Newton method for this purpose. In the next section, we give a precise definition of a suitably parameterized version T of $\mathcal{T}$ and establish its Fréchet differentiability.

4. The Fréchet derivative of T

Introducing the set of admissible parameterizations,

$$\mathcal{P} := \{p \in C^2([0,1],\Omega) \mid p([0,1]) \text{ is simple and } p'(t) \neq 0 \text{ for all } t \in [0,1]\},$$

which is an open subset of $C^2([0,1],\mathbb{R}^3)$, we assume from now on that K is parameterized by $p_K \in \mathcal{P}$. By simple, we mean here non-self-intersecting (possibly closed) curves. Therewith, we write (8) in the parameterized form

$$g_{\varepsilon,p_K} := \varepsilon^2\pi \int_0^1 (\gamma_0 - \kappa)\nabla N(p_K(t),\,\cdot\,)\cdot \mathbb{M}_{p_K}(t)\nabla u_0(p_K(t))|{p_K}'(t)|\,\mathrm{d}t, \quad (11)$$

where $\mathbb{M}_{p_K} := \mathbb{M}_K \circ p_K$ is the parameterized version of the polarization tensor corresponding to the family of conductivity inhomogeneities γ_ε, $0 < \varepsilon \leqslant \varepsilon_0$, around K as in (2). We consider in the following the nonlinear operator

$$T : \mathcal{P} \to L^2_\diamond(\partial\Omega), \qquad T(p) := g_{\varepsilon,p}, \quad (12)$$

where $g_{\varepsilon,p}$ is defined analogously to (11), involving a polarization tensor $\mathbb{M}_p$ corresponding to thin tubular conductivity inhomogeneities around the curve $p([0,1])$ as in (1) and (2).

To study this operator, we first note that for a C^2-curve parameterized by $p \in \mathcal{P}$, a parameterized unit tangent vector field along this curve is given by $\boldsymbol{t}_p := p'/|p'|$ and it can be completed to a continuous orthogonal frame $\{\boldsymbol{t}_p, \boldsymbol{n}_p, \boldsymbol{b}_p\}$. For instance, if $p'(t) \times p''(t) \neq 0$ for all $t \in [0,1]$, we can choose

$$\boldsymbol{t}_p := \frac{p'}{|p'|}, \quad \boldsymbol{n}_p := \frac{(p' \times p'') \times p'}{|(p' \times p'') \times p'|} \quad \text{and} \quad \boldsymbol{b}_p := \boldsymbol{t}_p \times \boldsymbol{n}_p = \frac{p' \times p''}{|p' \times p''|}.$$

Recalling the spectral properties of the polarization tensor, we can use this frame to diagonalize $\mathbb{M}_p$. More precisely, introducing the diagonal matrix $M := \mathrm{diag}(1, 2\gamma_0/(\gamma_0+\kappa), 2\gamma_0/(\gamma_0+\kappa)) \in \mathbb{R}^{3\times 3}$ and the matrix-valued function $V_p := [\boldsymbol{t}_p, \boldsymbol{n}_p, \boldsymbol{b}_p] \in C([0,1],\mathbb{R}^{3\times 3})$ defined column by column, we find that

$$\mathbb{M}_p(t) = V_p(t) M V_p^\top(t) \qquad \text{for} \quad t \in [0,1].$$

Lemma 4.1. *The mapping $p \mapsto \mathbb{M}_p$ is Fréchet differentiable from $\mathcal{P}$ into $C([0,1],\mathbb{R}^{3\times 3})$, and its Fréchet derivative at $p \in \mathcal{P}$ is given by $h \mapsto \mathbb{M}'_{p,h}$ with*

$$\mathbb{M}'_{p,h} := V'_{p,h} M V_p^\top + V_p M {V'_{p,h}}^\top, \quad (13)$$

where the matrix-valued function $V'_{p,h}$ is given columnwise by

$$V'_{p,h} := \frac{1}{|p'|}[(h'\cdot\boldsymbol{n}_p)\boldsymbol{n}_p + (h'\cdot\boldsymbol{b}_p)\boldsymbol{b}_p,\ -(h'\cdot\boldsymbol{n}_p)\boldsymbol{t}_p,\ -(h'\cdot\boldsymbol{b}_p)\boldsymbol{t}_p]. \quad (14)$$

Proof. Fix an arbitrary $p \in \mathcal{P}$ and let $\delta > 0$ be small enough such that $p + h \in \mathcal{P}$ for all $h \in C^2([0,1],\mathbb{R}^3)$ satisfying $\|h\|_{C^2([0,1],\mathbb{R}^3)} \leqslant \delta$. Suppose that h is such a small perturbation and denote by $\mathbb{M}_{p+h}$ the parameterized version of the polarization tensor corresponding to conductivity inhomogeneities as in (2) around the curve specified by $p + h$. Then, it can be seen straightforwardly that

$$\boldsymbol{t}_{p+h} = \frac{p' + h'}{|p' + h'|}, \quad (15a)$$

$$\boldsymbol{n}_{p+h} = (\boldsymbol{t}_p \cdot \boldsymbol{t}_{p+h})\boldsymbol{n}_p - \frac{\boldsymbol{b}_p \cdot \boldsymbol{t}_{p+h}}{1 + \boldsymbol{t}_p \cdot \boldsymbol{t}_{p+h}}(\boldsymbol{t}_p \times \boldsymbol{t}_{p+h}) - (\boldsymbol{n}_p \cdot \boldsymbol{t}_{p+h})\boldsymbol{t}_p, \quad (15b)$$

$$\boldsymbol{b}_{p+h} = (\boldsymbol{t}_p \cdot \boldsymbol{t}_{p+h})\boldsymbol{b}_p + \frac{\boldsymbol{n}_p \cdot \boldsymbol{t}_{p+h}}{1 + \boldsymbol{t}_p \cdot \boldsymbol{t}_{p+h}}(\boldsymbol{t}_p \times \boldsymbol{t}_{p+h}) - (\boldsymbol{b}_p \cdot \boldsymbol{t}_{p+h})\boldsymbol{t}_p \tag{15c}$$

define a continuous orthogonal frame along this perturbed curve. Using Taylor's formula, we deduce that

$$\begin{aligned}\boldsymbol{t}_{p+h} &= \boldsymbol{t}_p + \frac{1}{|p'|}h' - \frac{h' \cdot \boldsymbol{t}_p}{|p'|}\boldsymbol{t}_p + O\big(\|h\|^2_{C^2([0,1],\mathbb{R}^3)}\big) \\ &= \boldsymbol{t}_p + \frac{1}{|p'|}\big((h' \cdot \boldsymbol{n}_p)\boldsymbol{n}_p + (h' \cdot \boldsymbol{b}_p)\boldsymbol{b}_p\big) + O\big(\|h\|^2_{C^2([0,1],\mathbb{R}^3)}\big).\end{aligned}$$

Substituting this expression into (15), it follows that

$$\begin{aligned}\boldsymbol{n}_{p+h} &= \boldsymbol{n}_p - \frac{1}{|p'|}(h' \cdot \boldsymbol{n}_p)\boldsymbol{t}_p + O\big(\|h\|^2_{C^2([0,1],\mathbb{R}^3)}\big), \\ \boldsymbol{b}_{p+h} &= \boldsymbol{b}_p - \frac{1}{|p'|}(h' \cdot \boldsymbol{b}_p)\boldsymbol{t}_p + O\big(\|h\|^2_{C^2([0,1],\mathbb{R}^3)}\big),\end{aligned}$$

and thus

$$\|V_{p+h} - V_p - V'_{p,h}\|_{C([0,1],\mathbb{R}^{3\times 3})} \leqslant C\|h\|^2_{C^2([0,1],\mathbb{R}^3)}.$$

Here and throughout, C denotes a generic constant, the value of which might change at different occurrences. Consequently,

$$\|\mathbb{M}_{p+h} - \mathbb{M}_p - \mathbb{M}'_{p,h}\|_{C([0,1],\mathbb{R}^{3\times 3})} \leqslant C\|h\|^2_{C^2([0,1],\mathbb{R}^3)}, \tag{16}$$

which ends the proof. □

Theorem 4.2. *The operator T from (12) is Fréchet differentiable and its Fréchet derivative is given by $T' : \mathcal{P} \times C^2([0,1];\mathbb{R}^3) \to L^2_\diamond(\partial\Omega)$,*

$$T'(p,h) := \varepsilon^2\pi(\gamma_0 - \kappa)\big(T'_1(p,h) + T'_2(p,h) + T'_3(p,h) + T'_4(p,h)\big) \tag{17}$$

with

$$\begin{aligned}T'_1(p,h) &:= \int_0^1 h(t) \cdot D^2_x N(p(t),\cdot)\mathbb{M}_p(t)\nabla u_0(p(t))|p'(t)|\,\mathrm{d}t, \\ T'_2(p,h) &:= \int_0^1 \nabla_x N(p(t),\cdot) \cdot \mathbb{M}'_{p,h}(t)\nabla u_0(p(t))|p'(t)|\,\mathrm{d}t, \\ T'_3(p,h) &:= \int_0^1 \nabla_x N(p(t),\cdot) \cdot \mathbb{M}_p(t)D^2 u_0(p(t))h(t)|p'(t)|\,\mathrm{d}t, \\ T'_4(p,h) &:= \int_0^1 \nabla_x N(p(t),\cdot) \cdot \mathbb{M}_p(t)\nabla u_0(p(t))\frac{p'(t) \cdot h'(t)}{|p'(t)|}\,\mathrm{d}t.\end{aligned}$$

Here, $D^2_x N$ and $D^2 u_0$ denote the Hessian of N (with respect to the first variable) and u_0, respectively.

Proof. Let $p \in \mathcal{P}$, $\delta > 0$ and $h \in C^2([0,1],\mathbb{R}^3)$ be as in the proof of lemma 4.1; note, in particular, that there exists an open set Ω_0 such that $\overline{\Omega}_0 \subset \Omega$ and $(p+h)([0,1]) \subset \Omega_0$ for any feasible h, because the distance of $p([0,1])$ from $\partial\Omega$ is strictly larger than δ. Then, we have to show that

$$\lim_{h\to 0} \frac{1}{\|h\|_{C^2([0,1],\mathbb{R}^3)}} \big\|T(p+h) - T(p) - T'(p,h)\big\|_{L^2_\diamond(\partial\Omega)} = 0. \tag{18}$$

For this purpose, we divide $T(p+h) - T(p)$ into four parts:

$$T(p+h) - T(p) = \varepsilon^2 \pi(\gamma_0 - \kappa)\big(Q_1(p,h) + Q_2(p,h) + Q_3(p,h) + Q_4(p,h)\big), \tag{19}$$

where

$$Q_1(p,h) := \int_0^1 (\nabla_x N((p+h)(t),\cdot) - \nabla_x N(p(t),\cdot)) \cdot \mathbb{M}_{p+h}(t) \nabla u_0((p+h)(t)) \big|(p+h)'(t)\big| \,\mathrm{d}t,$$

$$Q_2(p,h) := \int_0^1 \nabla_x N(p(t),\cdot) \cdot (\mathbb{M}_{p+h}(t) - \mathbb{M}_p(t)) \nabla u_0((p+h)(t)) \big|(p+h)'(t)\big| \,\mathrm{d}t,$$

$$Q_3(p,h) := \int_0^1 \nabla_x N(p(t),\cdot) \cdot \mathbb{M}_p(t) \big(\nabla u_0((p+h)(t)) - \nabla u_0(p(t))\big) \big|(p+h)'(t)\big| \,\mathrm{d}t,$$

$$Q_4(p,h) := \int_0^1 \nabla_x N(p(t),\cdot) \cdot \mathbb{M}_p(t) \nabla u_0(p(t)) \big(|(p+h)'(t)| - |p'(t)|\big) \,\mathrm{d}t.$$

Considering each of these four terms separately, we first observe that for all $y \in \partial\Omega$, the Neumann function $N(\,\cdot\,, y)$ is smooth in $\Omega_0 \subset\subset \Omega$ and therefore Taylor's theorem implies that

$$\big\| \nabla_x N((p+h)(\cdot), y) - \nabla_x N(p(\cdot), y) - D_x^2 N(p(\cdot), y) h(\cdot) \big\|_{C([0,1],\mathbb{R}^3)} \leqslant C \|h\|^2_{C^2([0,1],\mathbb{R}^3)}$$

uniformly with respect to $y \in \partial\Omega$. Similarly, elliptic regularity results (cf, e.g., [18, chapter 2, theorem 3.2]) guarantee that u_0 is smooth in Ω_0; in particular,

$$\big\| \nabla u_0((p+h)(\cdot)) - \nabla u_0(p(\cdot)) - D^2 u_0(p(\cdot)) h(\cdot) \big\|_{C([0,1],\mathbb{R}^3)} \leqslant C \|h\|^2_{C^2([0,1],\mathbb{R}^3)}. \tag{20}$$

Finally, using Taylor's theorem once more, we find that

$$\left\| |p' + h'| - |p'| - \frac{p' \cdot h'}{|p'|} \right\|_{C([0,1],\mathbb{R}^3)} \leqslant C \|h\|^2_{C^2([0,1],\mathbb{R}^3)}. \tag{21}$$

Combining these estimates together with (16), it is straightforward to show that

$$\|Q_j(p,h) - T_j'(p,h)\|_{C(\partial\Omega)} \leqslant C \|h\|^2_{C^2([0,1],\mathbb{R}^3)} \qquad \text{for} \quad j = 1, \ldots, 4, \tag{22}$$

so that (18) follows from the triangle inequality after embedding $C(\partial\Omega)$ continuously into $L^2(\Omega)$. We prove (22) for $j = 2$ only and note that the other three cases follow similarly. By adding and subtracting a suitable term and using the triangle inequality, we deduce that

$$\|Q_2(p,h) - T_2'(p,h)\|_{C(\partial\Omega)} \leqslant \|Q_{21}(p,h)\|_{C(\partial\Omega)} + \|Q_{22}(p,h)\|_{C(\partial\Omega)}, \tag{23}$$

where

$$Q_{21}(p,h) = \int_0^1 \nabla_x N(p(t),\cdot) \cdot (\mathbb{M}_{p+h}(t) - \mathbb{M}_p(t)) \times (\nabla u_0((p+h)(t)) |(p+h)'(t)| - \nabla u_0(p(t)) |p'(t)|) \,\mathrm{d}t,$$

$$Q_{22}(p,h) = \int_0^1 \nabla_x N(p(t),\cdot) \cdot ((\mathbb{M}_{p+h}(t) - \mathbb{M}_p(t)) - \mathbb{M}'_{p,h}(t)) \nabla u_0(p(t)) |p'(t)| \,\mathrm{d}t.$$

From (13) and (14), we find that

$$\|\mathbb{M}'_{p,h}\|_{C([0,1],\mathbb{R}^{3\times 3})} \leqslant C \|h\|_{C^2([0,1],\mathbb{R}^3)}. \tag{24}$$

Thus, using the estimates (24), (20), (21), (16), and the boundedness of the derivatives of u_0

in Ω_0, it follows that

$$\|Q_{2j}(p,h)\|_{C(\partial\Omega)} \leqslant C\|h\|^2_{C^2([0,1],\mathbb{R}^3)} \max_{y\in\partial\Omega} \int_0^1 \left|\nabla_x N(p(t),y)\right| \mathrm{d}t \leqslant C\|h\|^2_{C^2([0,1],\mathbb{R}^3)}$$

for $j = 1, 2$, where the second inequality is a consequence of the boundedness of $\nabla_x N(\,\cdot\,,\,\cdot\,)$ on the compact set $p([0,1]) \times \partial\Omega$. Substituting these estimates into (23) completes the proof. □

Remark 4.3. The above proof readily shows that T remains continuously Fréchet differentiable even if its range is considered as a subspace of $C(\partial\Omega)$. Moreover, the corresponding Fréchet derivative is still given by the same formula (17). This fact will be utilized in the implementation of our reconstruction algorithm in the following section.

Remark 4.4. In section 5, we will build a numerical algorithm that does not only aim at reconstructing the base curve of a tubular inhomogeneity embedded in Ω but also the background conductivity level $\gamma_0 > 0$. For this reason, we will occasionally interpret T as a function of two variables by writing

$$T : \mathcal{P} \times \mathbb{R}_+ \to L^2_\diamond(\partial\Omega), \qquad T(p,\gamma_0) := g_{\varepsilon,p},$$

where $g_{\varepsilon,p}$ is defined analogously to (11). Take note that T, as well as T', does not depend on γ_0 merely through the term $\gamma_0 - \kappa$ and the polarization tensor but also via the implicit dependence of u_0 and the Neumann function on the background conductivity. In our reconstruction algorithm, we need to be able to differentiate T with respect to γ_0. Taking into account how $N(\,\cdot\,,\,\cdot\,)$ and u_0 scale with respect to γ_0, a simple calculation reveals that for a fixed p such a derivative can be written in $L^2_\diamond(\partial\Omega)$ as

$$\begin{aligned}\frac{\partial T(p,\gamma_0)}{\partial\gamma_0} &= \varepsilon^2\pi \int_0^1 \Big(2\frac{\kappa}{\gamma_0} - 1\Big)\nabla N(p(t),\,\cdot\,)\cdot\mathbb{M}_p(t)\nabla u_0(p(t))|p'(t)|\,\mathrm{d}t \\ &\quad + \varepsilon^2\pi \int_0^1 (\gamma_0-\kappa)\nabla N(p(t),\,\cdot\,)\cdot\frac{\partial\mathbb{M}_p(t)}{\partial\gamma_0}\nabla u_0(p(t))|p'(t)|\,\mathrm{d}t, \end{aligned} \tag{25}$$

where

$$\frac{\partial\mathbb{M}_p(t)}{\partial\gamma_0} = V_p(t)\frac{\partial M}{\partial\gamma_0}V_p^\top(t)$$

and

$$\frac{\partial M}{\partial\gamma_0} := \mathrm{diag}\big(0, 2\kappa/(\gamma_0+\kappa)^2, 2\kappa/(\gamma_0+\kappa)^2\big).$$

5. The reconstruction method

We assume that sufficiently good *a priori* knowledge of the radius ε and the conductivity κ of the tubular inclusion embedded in Ω are available in advance, which corresponds to having accurate information on the properties of the tubular material in question.

Our aim is to introduce an iterative Newton-type algorithm for reconstructing a thin tubular conductivity inhomogeneity by minimizing in a regularized manner the 'output least-squares' functional

$$\|(u_\varepsilon - u_0) - \mathcal{T}(K)\|_{L^2(\partial\Omega)} \tag{26}$$

with respect to K living in some set of feasible curves. As always, u_ε denotes the electromagnetic potential corresponding to the object contaminated by the target

inhomogeneity, i.e. the solution of (3) for some given boundary current density $f \in L^2_\diamond(\partial\Omega)$, and u_0 is the associated background potential. The nonlinear operator $\mathcal{T} : K \mapsto g_{\varepsilon,K}$ is defined by (10). Due to the asymptotic character of $g_{\varepsilon,K}$, the value of (26) is small—but in general nonzero—if K is the actual curve defining the unknown tubular inclusion within Ω (cf example 2.2).

To be able to minimize the functional (26), one must first introduce some suitable parameterization for K. As mentioned before, we choose to work with piecewise linear curves of the form

$$K = K(x^1, \ldots, x^{n+1}) = \bigcup_{j=1}^{n} [x^j, x^{j+1}],$$

where $x^1, \ldots, x^{n+1} \in \Omega$ is a set of nodal points and $[x^j, x^{j+1}]$ denotes the closed line segment between x^j and x^{j+1}.

Besides a parameterization for the candidate curves, a successful implementation of an iterative Newton-type output least-squares algorithm requires an appropriately chosen form of regularization. Intuitively, there are two types of behaviors that we want to avoid: (i) the piecewise linear approximation must not get severely tangled and (ii) none of its subsegments should become very short or extremely long. With this picture in mind, we introduce two penalty terms:

$$\Psi_1(x^1, \ldots, x^{n+1}) = n \sum_{j=1}^{n-1} |\boldsymbol{t}_{j+1} - \boldsymbol{t}_j|^2, \qquad \Psi_2(x^1, \ldots, x^{n+1}) = n \sum_{j=1}^{n} \left| d - |x^{j+1} - x^j| \right|^2,$$

where $\boldsymbol{t}_j \in \mathbb{R}^3$ is the unit tangent of the line segment $[x^j, x^{j+1}]$ pointing in the direction of x^{j+1}, and $d > 0$ is chosen so that $L = nd$ equals our *a priori* estimate for the total length of the unknown tubular inhomogeneity. The first of these functionals takes large values if the directions of adjacent subsegments of K differ substantially. Up to multiplication by a constant that is independent of n, the value $\Psi_1(x^1, \ldots, x^{n+1})$ can actually be seen as an estimate for the mean of the squared curvature of a smooth curve passing through the nodes $x^1, \ldots, x^{n+1}$, under the assumption that all subsegments $[x^j, x^{j+1}]$, $j = 1, \ldots, n$, are of equal length. In particular, this means that Ψ_1 is to a certain extent independent of the level of discretization n. On the other hand, the second penalty functional promotes curves that are composed of subsegments of equal length. Like Ψ_1, also Ψ_2 scales appropriately with respect to n: for a piecewise linear curve that is composed of subsegments of equal length, the value of Ψ_2 depends only on the total length of the curve in question, not on the number of its subsegments. Take note that both Ψ_1 and Ψ_2, as well as their derivatives, can be written as explicit functions of the nodes $x^1, \ldots, x^{n+1}$, but neither of them is quadratic with respect to the coordinates of $x^1, \ldots, x^{n+1}$.

Combining the output least-squares functional (26) with the two penalty terms Ψ_1 and Ψ_2 would suffice for devising a Newton-type reconstruction algorithm if γ_0 was assumed to be known. However, since the constant background conductivity is not typically available with high precision in practice, we include its estimation as a part of our reconstruction algorithm. Not knowing γ_0 unfortunately means that we cannot compute u_0 needed in the functional (26), and thus we must come up with an alternative scheme: let $u_{\mathbf{1}}$ be the background solution in the case that $\gamma_0 \equiv 1$ and note that the potential u_σ corresponding to a general constant conductivity $\sigma > 0$—and the same boundary current density f—has the representation

$$u_\sigma = \frac{u_{\mathbf{1}}}{\sigma}. \tag{27}$$

We substitute u_σ given by (27) for u_0 and σ for γ_0 in (26) and treat σ as another unknown; note that the operator $\mathcal{T}$ in (26) also depends now on σ (cf remark 4.4). After introducing a

quadratic penalty term acting on σ and combining it with (26) and the penalty functionals Ψ_1 and Ψ_2, we finally end up with a suitable regularized output least-squares functional

$$F(x^1,\dots,x^{n+1},\sigma) = \left\| \left(u_\varepsilon - \frac{u_{\mathbf{1}}}{\sigma}\right) - \sum_{j=1}^{n} \mathcal{T}\left([x^j, x^{j+1}], \sigma\right) \right\|^2_{L^2(\partial\Omega)} + \lambda_1^2 \Psi_1(x^1,\dots,x^{n+1}) + \lambda_2^2 \Psi_2(x^1,\dots,x^{n+1}) + \lambda_3^2(\tilde{\sigma}-\sigma)^2, \tag{28}$$

where $\tilde{\sigma} > 0$ is our initial guess for the constant background conductivity and $\lambda_m > 0$, $m = 1, 2, 3$, are regularization parameters to be specified later on.

Before introducing the actual reconstruction algorithm, we must still discretize the $L^2(\partial\Omega)$-norm appearing in (28). For this purpose, we assume that Ω is the unit ball, which is also the framework adopted for the numerical studies of section 6, but note that more general geometries can be treated similarly (see also remark 2.3). Suppose that we can measure or interpolate the boundary potential $u_\varepsilon|_{\partial\Omega}$ on a grid of points $y_{kl} \in \partial\Omega$, $1 \leqslant k \leqslant N-1$ and $1 \leqslant l \leqslant 2N$, as introduced in (7); then, the trapezoidal rule gives the following approximation for F:

$$F_N(x^1,\dots,x^{n+1},\sigma) = \frac{\pi^2}{N^2} \sum_{k,l} \sin\theta_k \left| \left(\left(u_\varepsilon - \frac{u_{\mathbf{1}}}{\sigma}\right) - \sum_{j=1}^{n} \mathcal{T}\left([x^j, x^{j+1}], \sigma\right) \right)(y_{kl}) \right|^2 + \lambda_1^2 \Psi_1(x^1,\dots,x^{n+1}) + \lambda_2^2 \Psi_2(x^1,\dots,x^{n+1}) + \lambda_3^2(\tilde{\sigma}-\sigma)^2, \tag{29}$$

which is what we aim to minimize in our reconstruction algorithm. By slight abuse of notation, F_N can be written in the form

$$F_N(\eta) = |r(\eta)|^2,$$

where $\eta \in \mathbb{R}^{3n+4}$ is a parameter vector that is composed of the estimate for the background conductivity and the components of the nodal points of the piecewise linear candidate curve, and $r : \mathbb{R}^{3n+4} \to \mathbb{R}^{2N(N-1)+2n}$ is a nonlinear vector-valued function of η. Our algorithm minimizes $F_N(\eta)$ using a mixture of the Gauss–Newton algorithm and the golden section line search method. In what follows, we denote the Jacobian of r by J_r.

Algorithm 5.1. Choose the parameters n, d, λ_1, λ_2, λ_3 and $\tilde{\sigma}$ for the functional F_N and pick an initial guess $\eta_0 \in \mathbb{R}^{3n+4}$ that defines a piecewise linear curve in Ω and a positive background conductivity. Set $k = 0$, choose $0 < \delta < 1$ and $M \in \mathbb{N}$, and iterate as follows.

Compute a Gauss–Newton search direction

$$\Delta_k = -\left(J_r^\top(\eta_k) J_r(\eta_k)\right)^{-1} J_r^\top(\eta_k) r(\eta_k), \tag{30}$$

and denote by $t_{\max} > 0$ the largest real number for which $\eta_k + t_{\max}\Delta_k$ defines a piecewise linear curve in $\overline{\Omega}$ and a nonnegative constant conductivity. Find the minimizer t_k of the function $t \mapsto F_N(\eta_k + t\Delta_k)$ on the interval $[0, \delta t_{\max}]$ by using the golden section line search with M divisions. If $t_k > 0$, set $\eta_{k+1} = \eta_k + t_k\Delta_k$ and $k = k+1$, and continue the iteration by computing a new search direction. Otherwise, terminate the algorithm and declare the piecewise linear curve and the constant conductivity parameterized by the current iterate η_k as the reconstruction.

To compute J_r needed in the above algorithm, one has to differentiate the terms on the right-hand side of (29) with respect to σ and the components of the nodal points $x^1,\dots,x^{n+1}$. The terms that depend on σ are the corresponding penalty function, $u_{\mathbf{1}}/\sigma$, and $\mathcal{T}([x^j, x^{j+1}], \sigma)$. The first two of these cause no problems whatsoever and the derivative of the third one can be computed by applying, say, the trapezoidal rule to the integrals on the right-hand side of (25)—with u_0 replaced by u_σ and using the Neumann function corresponding to the current

estimate for the conductivity level (cf (4)). On the other hand, all derivatives of Ψ_1 and Ψ_2 with respect to the nodal points of the approximating curve can be calculated explicitly. In consequence, the only unsettled issue is the differentiation of $\mathcal{T}\big([x^j, x^{j+1}]\big)(y_{kl})$, $j = 1, \ldots, n$, with respect to the components of nodal points x^j and x^{j+1}.

With the help of theorem 4.2 and remark 4.3—see also remark 4.4—it is straightforward to deduce that

$$\frac{\partial \mathcal{T}([x^j, x^{j+1}], \sigma)}{\partial x_m^j}(y_{kl}) = T'(([x^j, x^{j+1}], \sigma), h)(y_{kl}), \qquad m = 1, 2, 3, \quad (31)$$

for $h(t) = (1-t)\,\mathbf{e}_m$, $t \in [0, 1]$, where $\mathbf{e}_m$ is the mth standard basis vector in $\mathbb{R}^3$. On the right-hand side, $[x^j, x^{j+1}]$ is to be identified with its linear parameterization with respect to $t \in [0, 1]$ starting from x^j, i.e. $p(t) = (1-t)x^j + tx^{j+1}$. Similarly, the derivative with respect to x_m^{j+1} is obtained by choosing $h(t) = t\mathbf{e}_m$ in (31). In the numerical implementation of the algorithm, the needed point values of these derivatives as well as those of the original operator $\mathcal{T}$ are computed by applying the trapezoidal rule with sufficiently many nodal points to the integrals (17) and (11), respectively.

Finally, we note that the golden section line search employed in algorithm 5.1 is guaranteed to converge only if the target function is convex. In our case, there is no guarantee of convexity, but in practically all tests that we have carried out $F_N(\eta_k)$ has anyway decreased monotonically as a function of the iteration step k. Moreover, in none of our numerical experiments did we encounter any difficulties when inverting the matrix $J_r^\top(\eta_k)J_r(\eta_k)$ in (30).

6. Numerical results

In this section we test the functionality of algorithm 5.1 in the unit ball with both exact and noisy simulated data. In all numerical studies, we use

$$f(x) = \nu(x) \cdot (1, 0, 0) = x_1, \qquad x \in \partial\Omega,$$

as the boundary current density and recall that for this choice, the potential corresponding to the unit conductivity needed in (29) is simply $u_{\mathbf{1}} = x_1$. For each numerical test, we simulate the electromagnetic potential u_ε corresponding to the target tubular inhomogeneity at the measurement points (7) with $N = 10$ by solving problem (3) using the finite element software Comsol. The actual background conductivity is chosen to be $\gamma_0 \equiv 1$ in all of our tests.

Before moving on to the numerical experiments, let us fix the parameters appearing in algorithm 5.1. We will search for an approximation of the shape of the target inhomogeneity in the form of a piecewise linear curve composed of $n = 10$ subsegments. Note that this is in accordance with our findings in example 2.2, where we have seen that a higher number of subsegments does not significantly improve the approximation properties of our asymptotic model for inclusions of comparable dimensions. The length of the target inhomogeneity is anticipated to be $L = 1.5$, and thus we choose $d = 0.15$. In all numerical examples with exact data, i.e. without artificial additive noise, the regularization parameters are fixed as

$$\lambda_1 = 10^{-5}, \qquad \lambda_2 = 6 \cdot 10^{-5}, \qquad \lambda_3 = 0.08. \quad (32)$$

When working with noisy data, we multiply these values by 1.4. The initial guess for the background conductivity $\tilde{\sigma}$ varies from test to test: it is chosen to be the constant conductivity that minimizes the discrepancy

$$\sum_{k,l} \sin\theta_k \left| u_\varepsilon(y_{kl}) - \frac{u_{\mathbf{1}}(y_{kl})}{\sigma} \right|^2$$

over $\sigma > 0$, i.e. the constant conductivity that gives the best fit with the measured boundary data with respect to the $L^2(\partial\Omega)$-norm. We set $\delta = 0.99$ and use the golden section line search with $M = 10$ divisions at each iteration step of algorithm 5.1. Finally, in all of our tests, the initial guess for the nodal points $\{x^j\}_{j=1}^{n+1}$ is obtained by taking the line segment $[(0, -0.75, 0), (0, 0.75, 0)]$ parallel to the x_2-axis and dividing it into n subsegments of equal length.

6.1. Tests with exact data

Example 6.1. In our first test, the target inhomogeneity is the cylinder of radius $\varepsilon = 0.03$ and length 0.64 depicted in the top-left image of figure 2.

The conductivity inside the inclusion is $\kappa = 0.4$. The top-right image of figure 2 shows the reconstruction provided by algorithm 5.1; in this case, the iterations were terminated after 30 rounds. Apart from mild wriggling, the reconstruction coincides nicely with the target inhomogeneity. The bottom row of figure 2 visualizes the evolution of the reconstruction process: The left-hand image shows the initial guess for the tubular inhomogeneity together with three intermediate stages of the algorithm corresponding to the iterates $k = 1, 5$ and 12, respectively. The estimate for the background conductivity as a function of the iteration number is plotted in the bottom-right image. This first numerical example requires relatively many iteration steps because the piecewise linear approximation becomes folded during the first couple of iterations and it takes some time before it gets straightened out once again.

Example 6.2. The second numerical example considers a tubular inhomogeneity of radius $\varepsilon = 0.01$ and conductivity $\kappa = 10$ depicted in the top-left image of figure 3. It is composed of two circular arcs and has a total length of 1.41. In this case, algorithm 5.1 converged in 18 iterations. The resulting reconstruction, which coincides almost exactly with the target curve, is shown in the top-right image of figure 3. The bottom row of figure 3 visualizes the evolution of the algorithm. This time the bottom-left image shows the intermediate stages corresponding to the iterates $k = 1, 3$ and 8.

Example 6.3. Our third and final test with exact data considers reconstructing the tubular inclusion with $\varepsilon = 0.02$ and conductivity $\kappa = 2$ defined by the circle shown in the top-left image of figure 4. The radius of the circle is 0.4 and its arclength is thus 2.51. For this closed target curve, our algorithm converged after eight iterations. Although the corresponding reconstruction presented in the top-right image of figure 4 carries many characteristics of the target inclusion, it is not even close to being closed, and thus the performance of algorithm 5.1 cannot be considered totally satisfactory in this test case. The bottom row of figure 4 visualizes once again the reconstruction process: this time the shown intermediate iterates correspond to the values $k = 1, 2$ and 5. It is noteworthy that—unlike in the previous two examples—this time the estimate for the background conductivity does not quite converge to the correct value of $\gamma_0 = 1$.

Note that if it is known *a priori* that the unknown inclusion corresponds to a closed base curve K, the output least-squares functional F_N can be modified suitably such that the algorithm recovers closed piecewise linear splines only.

To sum up, our reconstruction algorithm provides reasonable results in all of the above test cases. We want to emphasize that for all three targets convergence to qualitatively similar reconstructions is observed also if the initial guess is chosen to be parallel to the x_1- or x_3-axis. The speed of convergence depends heavily on the initial guess, though. We also ran the above experiments with $n = 5$ and $n = 20$ subsegments and the same regularization

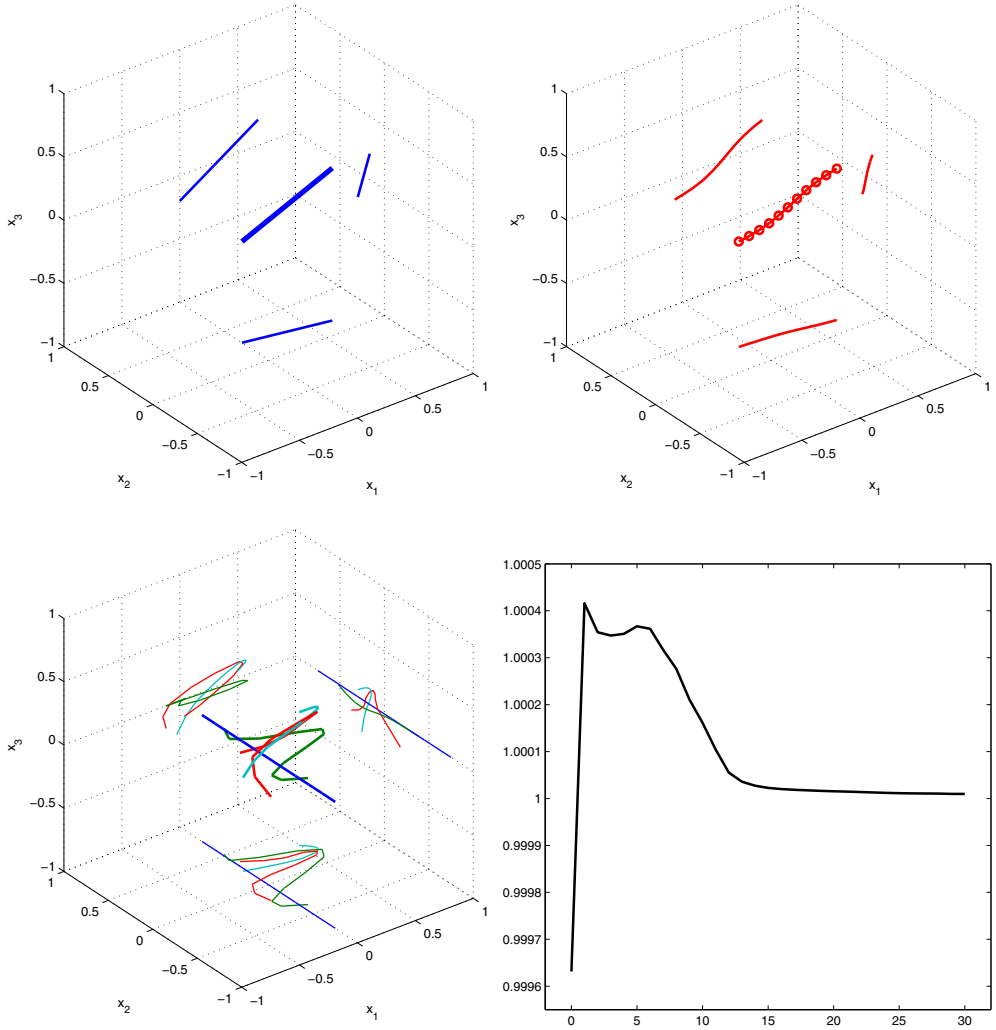

Figure 2. Top-left: the curve defining the target inhomogeneity with $\varepsilon = 0.03$ and $\kappa = 0.4$. Top-right: the reconstruction ($k = 30$). The small balls indicate the locations of the nodal points. Bottom-left: the initial guess (blue) and three intermediate reconstructions corresponding to the iterates $k = 1$ (green), $k = 5$ (red) and $k = 12$ (turquoise). Bottom-right: the estimate for the background conductivity as a function of the iteration number.

parameters, which resulted in reconstructions that were almost the same as the ones presented above, not taking into account the level of discretization of course. Even the needed number of iterations did not vary much with n. It is noteworthy that one can get better results for a particular target inhomogeneity by choosing the regularization parameters more specifically: with slightly smaller λ_1 and λ_2 that penalize less for twisting and the length of the piecewise linear approximation curve, the reconstruction corresponding to the toroidal inhomogeneity becomes better. This would, however, easily lead to a twofold reconstruction in the case of the cylindrical inclusion. Vice versa, larger λ_1 would make the reconstruction for the cylinder straighter, but such a choice would force the end points of the reconstruction corresponding

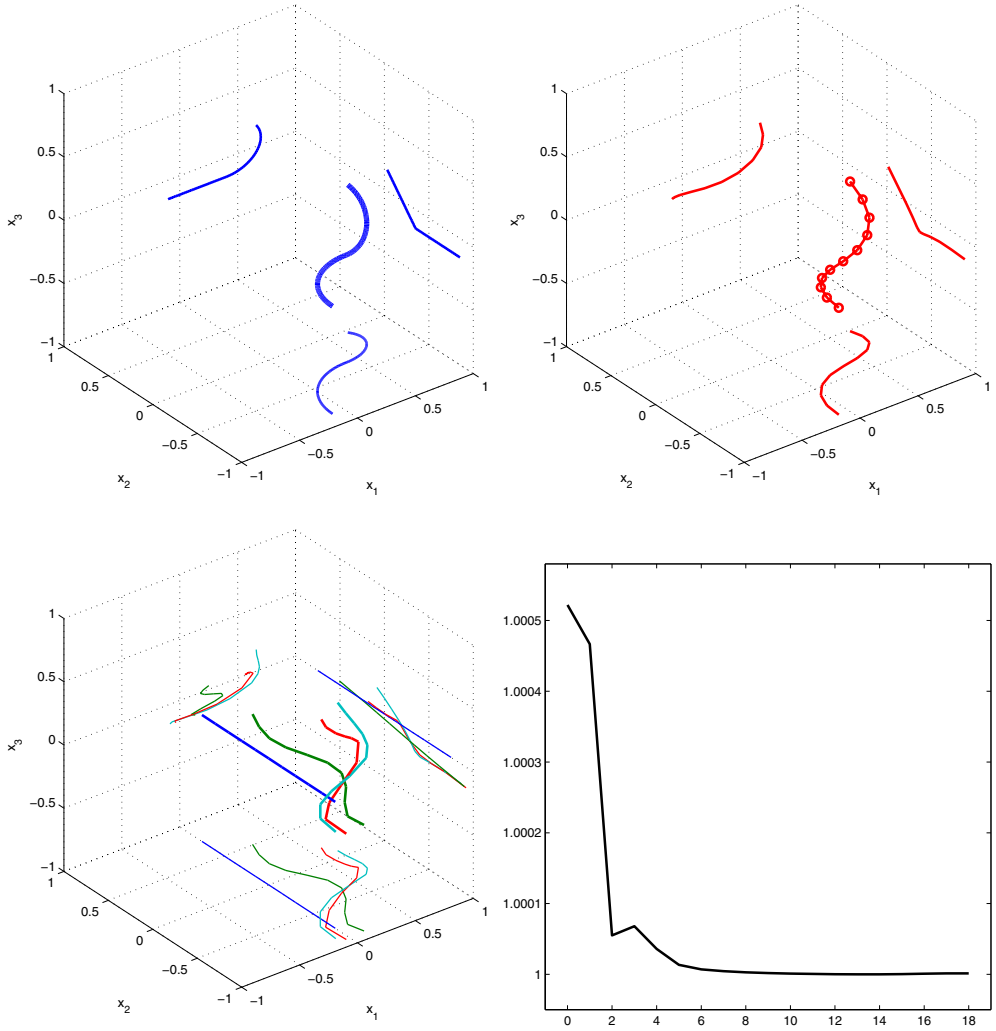

Figure 3. Top-left: the curve defining the target inhomogeneity with $\varepsilon = 0.01$ and $\kappa = 10$. Top right: the reconstruction ($k = 18$). The small balls indicate the locations of the nodal points. Bottom-left: the initial guess (blue) and three intermediate reconstructions corresponding to the iterates $k = 1$ (green), $k = 3$ (red) and $k = 8$ (turquoise). Bottom-right: the estimate for the background conductivity as a function of the iteration number.

to the torus to be even further apart. All in all, the regularization parameters listed in (32) seem to provide a relatively good compromise that works well for different types of tubular inhomogeneities and for different levels of discretization n.

6.2. Tests with noisy data

Next, we turn our attention to the case of noisy simulated data. Given a target inhomogeneity, we contaminate the point values of the solution to (3) needed for (29) with realizations of normally distributed random variable with zero mean and standard deviation 5×10^{-5}. This corresponds to a noise level of approximately 0.005% in the data $u_\varepsilon|_{\partial\Omega}$; recall that $u_0 = x_1$, which is of

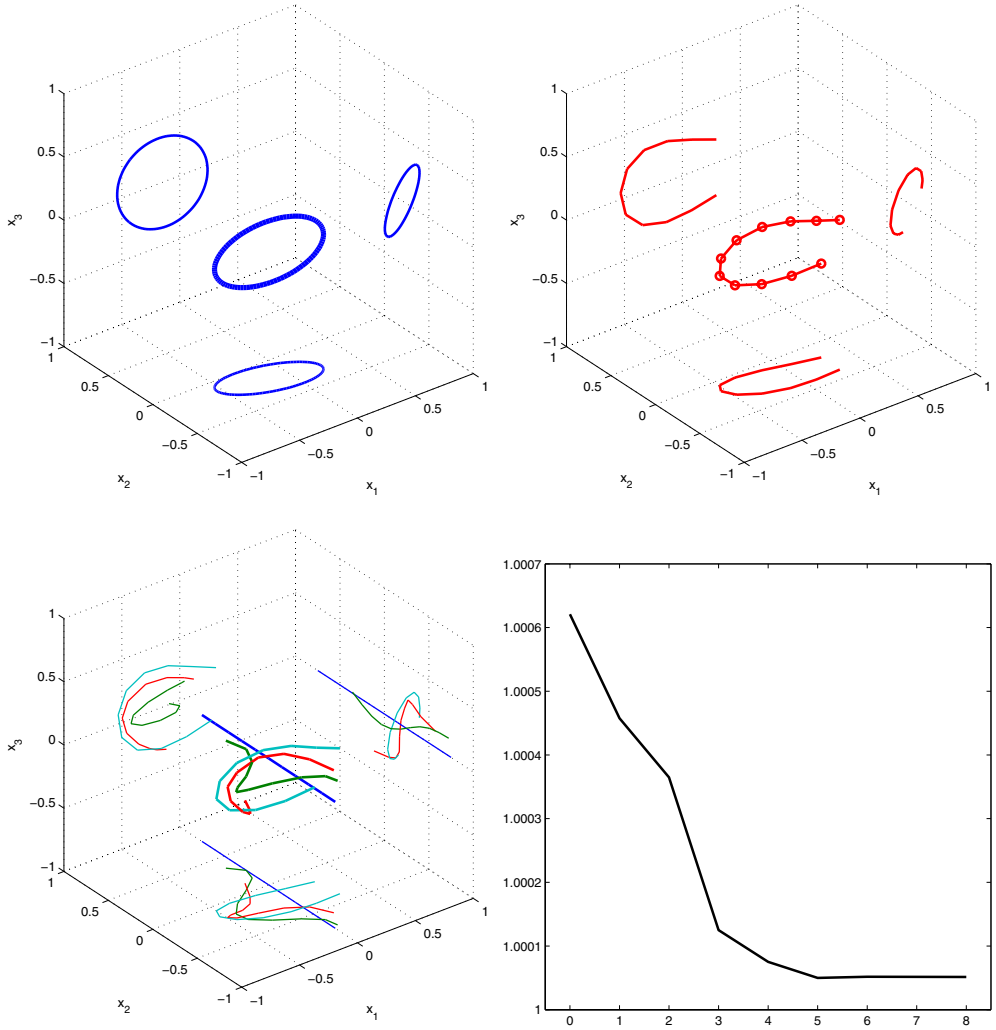

Figure 4. Top-left: the curve defining the target inhomogeneity with $\varepsilon = 0.02$ and $\kappa = 2$. Top-right: the reconstruction ($k = 8$). The small balls indicate the locations of the nodal points. Bottom-left: the initial guess (blue) and three intermediate reconstructions corresponding to the iterates $k = 1$ (green), $k = 2$ (red) and $k = 5$ (turquoise). Bottom-right: the estimate for the background conductivity as a function of the iteration number.

the same order of magnitude as u_ε. Although at first glance, this seems almost like working with exact measurements, the noise content of the relative boundary potential $(u_\varepsilon - u_0)|_{\partial\Omega}$ is in fact between 3% and 5% depending on the target inhomogeneity in question—thin tubular inhomogeneties do not affect boundary measurements very much.

Example 6.4. The reconstructions corresponding to noisy data and the three tubular inhomogeneities introduced in section 6.1 are presented in figure 5. For ease of comparison, the original target inhomogeneities are also shown in the top-left image. The reconstruction corresponding to the cylindrical inhomogeneity in the top-right image of figure 5 is almost as good as the corresponding one for exact data; in this case, the algorithm converged after

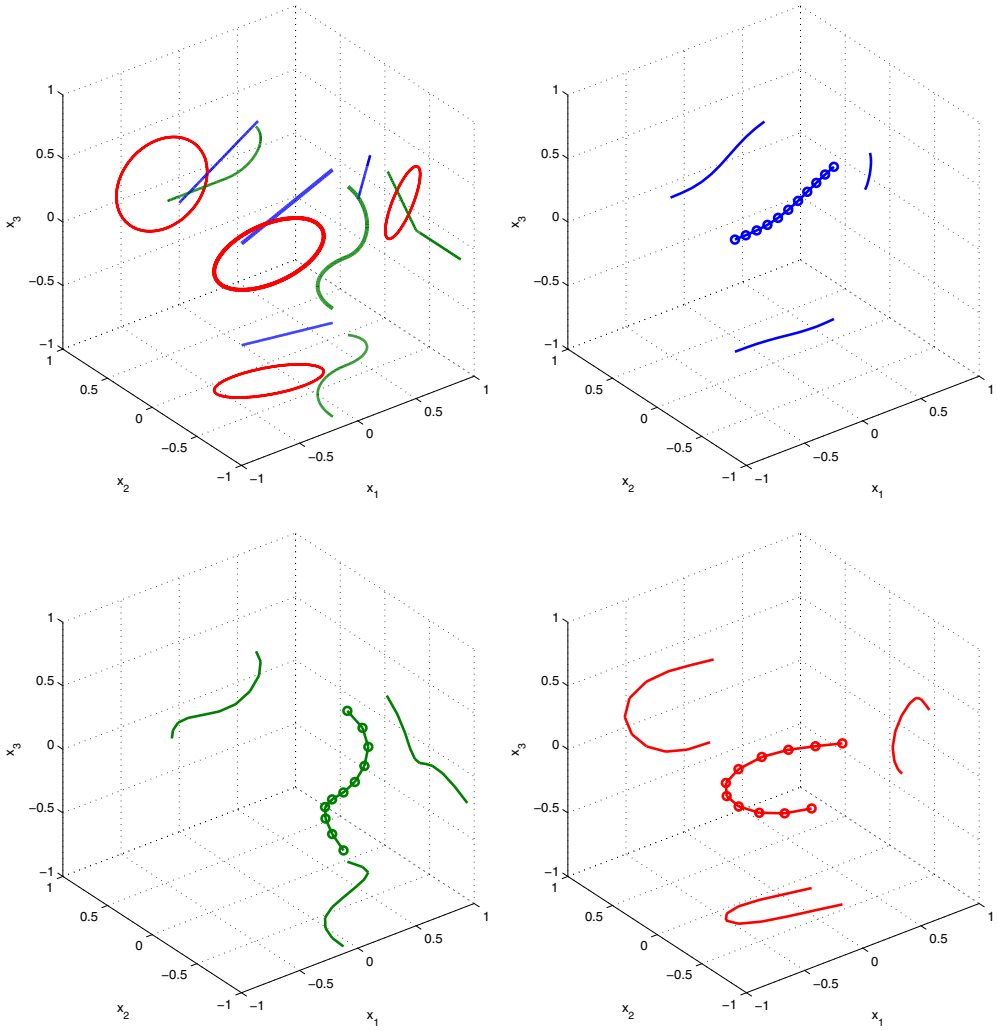

Figure 5. Top-left: the curves defining the target inhomogeneities. The other images show the reconstructions corresponding to noisy data. Top-right: the cylindrical target inhomogeneity ($k = 20$). Bottom-left: the target inhomogeneity composed of two circular arcs ($k = 19$). Bottom-right: the circular target inhomogeneity ($k = 15$).

20 iterations. The reconstructions of the curved and circular inhomogeneities in the bottom row of figure 5 were produced in 19 and 15 iterations, respectively. Both of them are clearly less accurate than the corresponding ones in the noiseless case, but arguably they carry useful information on the corresponding target inclusions anyway. We have not visualized the evolution of the reconstruction process in the case of noisy measurements because the resulting images would be qualitatively similar to the ones in figures 2, 3 and 4 for exact data.

The reconstructions provided by algorithm 5.1 using noisy data vary somewhat depending on the particular realization of noise and the orientation of the line segment serving as the initial guess. However, the results for the three target inhomogeneities are in most cases qualitatively similar to the ones presented in figure 5. The two most typical deteriorations

that we have encountered are that one of the two curves in the reconstruction of the bottom-left image of figure 5 is missing and that the ends of the reconstruction corresponding to the toroidal inclusion point even further apart. Sometimes the algorithm even gets stuck in a local minimum of the functional (29) and is only able to capture the approximate location of the target inclusion. The most notorious combination for such an unfortunate behavior is considering the curved inhomogeneity composed of two circular arcs and an initial guess that is parallel to the x_1-axis. Even after taking these flaws into account, one can still argue that algorithm 5.1 functions reasonably well even if the data are corrupted with a temperate amount of measurement noise.

Remark 6.5. Applying the Newton-type reconstruction scheme to the examples considered in [12], we found that the reconstructions corresponding to examples 5.2 and 5.3 of [12] are comparable to the reconstructions shown in examples 6.1 and 6.2. For the complicated inclusion considered in example 5.5 of [12], the Newton-type scheme yields the correct location and orientation but not the shape of the inclusion. This is not a surprise since the Newton-type scheme uses only one current-to-voltage pair, while the qualitative method requires the whole Neumann-to-Dirichlet map. The reconstruction of multiply connected conductivity inhomogeneities, as considered in example 5.4 of [12], would require an improved reconstruction algorithm that, e.g., allows for a multiply connected initial guess.

Concluding remarks

We discussed a regularized Newton-type scheme to reconstruct the position and shape of a thin tubular conductivity inhomogeneity inside a homogeneous three-dimensional body from a single measurement of electrostatic currents and potentials on its boundary; the estimation of the constant background conductivity of the body can also be included as a part of the introduced algorithm. The method is based on an explicit asymptotic perturbation formula for the boundary potential due to thin tubular inclusions, which allows for very fast evaluation of the output least-squares functional and of its Fréchet derivative in each step of the iteration process. Numerical experiments suggest that the method works reasonably well for non-closed tubular inclusions as long as a sufficiently good initial guess for the approximate position, the radius and the conductivity of the inclusion are available.

Comparing this method to the qualitative reconstruction method developed in [12], a clear disadvantage of the Newton-type method is its need for sufficiently good *a priori* information to obtain useful reconstructions. On the other hand, the Newton-type method is fast and uses much less data than the qualitative method from [12], which requires an approximation of the whole Neumann-to-Dirichlet map.

References

[1] Ammari H, Beretta E and Francini E 2004 Reconstruction of thin conductivity imperfections *Appl. Anal.* **83** 63–76

[2] Ammari H, Beretta E and Francini E 2006 Reconstruction of thin conductivity imperfections: II. The case of multiple segments *Appl. Anal.* **85** 87–105

[3] Beretta E, Capdeboscq Y, de Gournay F and Francini E 2009 Thin cylindrical conductivity inclusions in a 3-dimensional domain: a polarization tensor and unique determination from boundary data *Inverse Problems* **25** 065004

[4] Brühl M, Hanke M and Pidcock M 2001 Crack detection using electrostatic measurements *M2AN Math. Model. Numer. Anal.* **35** 595–605

[5] Bryan K and Vogelius M S 2004 A review of selected works on crack identification *Geometric Methods in Inverse Problems and PDE Control* ed C B Croke, I Lasiecka, G Uhlmann and M S Vogelius *(IMA Vol. Math. Appl.* vol 137*)* (New York: Springer) pp 25–46
[6] Cakoni F and Colton D 2003 The linear sampling method for cracks *Inverse Problems* **19** 279–95
[7] Capdeboscq Y and Vogelius M S 2003 A general representation formula for boundary voltage perturbations caused by internal conductivity inhomogeneities of low volume fraction *Math. Model. Numer. Anal.* **37** 159–73
[8] Capdeboscq Y and Vogelius M S 2003 Optimal asymptotic estimates for the volume of internal inhomogeneities in terms of multiple boundary measurements *Math. Model. Numer. Anal.* **37** 227–40
[9] Capdeboscq Y and Vogelius M S 2006 Pointwise polarization tensor bounds, and applications to voltage perturbations caused by thin inhomogeneities *Asymptotic Anal.* **50** 175–204
[10] Dautray R and Lions J L 1990 *Mathematical Analysis and Numerical Methods for Science and Technology (Physical Origins and Classical Methods* vol 1*)* (Berlin: Springer)
[11] Friedman A and Vogelius M S 1989 Identification of small inhomogeneities of extreme conductivity by boundary measurements: a theorem on continuous dependence *Arch. Ration. Mech. Anal.* **105** 299–326
[12] Griesmaier R 2010 Reconstruction of thin tubular inclusions in three-dimensional domains using electrical impedance tomography *SIAM J. Imaging Sci.* **3** 340–62
[13] Ivanyshyn O and Kress R 2008 Inverse scattering for planar cracks via nonlinear integral equations *Math. Methods Appl. Sci.* **31** 1221–32
[14] Kirsch A and Ritter S 2000 A linear sampling method for inverse scattering from an open arc *Inverse Problems* **16** 89–105
[15] Kress R 1995 Inverse scattering from an open arc *Math. Methods Appl. Sci.* **18** 267–93
[16] Kress R and Lee K-M 2003 Integral equation methods for scattering from an impedance crack *J. Comput. Appl. Math.* **161** 161–77
[17] Kress R and Serranho P 2005 A hybrid method for two-dimensional crack reconstruction *Inverse Problems* **21** 773–84
[18] Lions J-L and Magenes E 1972 *Non-Homogeneous Boundary Value Problems and Applications (Die Grundlehren der Mathematischen Wissenschaften* vol I*)* (New York: Springer)
[19] Park W-K and Lesselier D 2009 MUSIC-type imaging of a thin penetrable inclusion from its multi-static response matrix *Inverse Problems* **25** 075002
[20] Park W-K and Lesselier D 2009 Electromagnetic MUSIC-type imaging of perfectly conducting, arc-like cracks at single frequency *J. Comput. Phys.* **228** 8093–111
[21] Park W-K and Lesselier D 2009 Reconstruction of thin electromagnetic inclusions by a level-set method *Inverse Problems* **25** 085010